

Neutrino Studies and the SNO+ Experiment

Doctoral Candidacy Exam Report

Jie Hu

Department of Physics, University of Alberta

1. Introduction

1.1. Research Background

The neutrino is an elementary particle in the Standard Model. The Standard Model is a theory describing elementary particles and their interactions. It has successfully described and predicted particle physics for 40 years, including the discovery of Higgs bosons in 2012. In the Standard Model, neutrinos are created from weak interactions in one of three leptonic flavors: electron neutrinos (ν_e), muon neutrinos (ν_μ) and tauon neutrinos (ν_τ), accompanied by electrons (e), muons (μ) and tauons (τ) respectively[1]. However, some properties of neutrinos can not be described by the Standard Model, such as the neutrino mass, which shows clues of the new physics beyond the Standard Model. This puts the studies of neutrinos in the spotlight.

The SNO+ experiment will explore the unknown properties of neutrinos, by examining the nature of neutrinos: whether they are Majorana or Dirac particles.

1.2. Discovery of Neutrino

The existence of neutrinos was first put forward by Wolfgang Pauli in the 1930s to solve the contradictions observed in beta decay experiments. It was shown definitively by James Chadwick in 1914 that the electrons emitted in beta decay did not have a discrete set of energies but instead had a continuous spectrum[2]. This means that the energy, momentum and angular momentum (spin) were not conserved between the nucleus and electron. Pauli introduced a charge-neutral, spin-1/2 and nearly massless new particle. The sum of the energies of the new particle, the nucleus and electron is constant, which solved the problem.

In 1934, Bethe and Peierls suggested direct neutrino detection via a neutrino-induced interaction, the inverse beta decay (IBD): $\bar{\nu}_e + p \rightarrow e^+ + n$.

Their calculation showed that the IBD cross section was of the order of 10^{-44} cm 2 . Such a small cross section indicates that the neutrino is difficult to detect[3].

In 1956, Fred Reines and Clyde Cowan made the first discovery of the neutrino (specifically, it was electron antineutrinos $\bar{\nu}_e$) by using a nuclear reactor as an intense neutrino source with neutrino fluxes on the order of $10^{12} - 10^{13}$ neutrinos/second/cm 2 . The active volume of their detector was two tanks filled with water in which cadmium chloride (CdCl_2) was dissolved. The water tanks were surrounded by liquid scintillator layers coupled with photomultiplier tubes (PMT) to detect emitted photons. The incoming antineutrinos interacted with the water via IBD. The produced positrons quickly annihilated with e^- and gave γ signals while the produced neutrons went through the neutron capture process: $n + ^{108}\text{Cd} \rightarrow ^{109}\text{Cd}^* \rightarrow ^{109}\text{Cd} + \gamma$ and gave delayed γ signals. A coincidence of these two characteristic signals provided a distinctive signature for the neutrino reaction. They measured the cross-section as 6.3×10^{-44} cm 2 , which was consistent with Bethe's calculation[2, 4].

1.3. Solar Neutrino

In the 1930s, Bethe et al. explained the origin of the Sun's energy is a series of nuclear reactions[5].

Based on the available physics and experimental data, the Standard Solar Model (SSM) is a modern and accepted theory for the evolution of the Sun. The energy in the Sun is mainly produced by two classes of reactions: the proton-proton (pp) chain and the Carbon-Nitrogen-Oxygen (CNO) cycle. The result of the two reactions is: $4p + 2e^- \rightarrow ^4\text{He} + 2\nu_e + Q$, where the released energy, Q is 26.73 MeV. The ν_e produced in the Sun (the solar neutrinos) can be detected on the Earth[6].

Due to the branching ratios and unterminated chains in the pp chain and CNO cycle, the solar neutrinos come from different reactions, as shown in Table 1. The solar neutrinos detected on the Earth are named after the specific fusion process[7]. They have different fluxes and energies, as shown in Figure 1[8].

1.4. Early Solar Neutrino Experiments

In 1964, John Bahcall and Raymond Davis proposed the first experiment to detect solar neutrinos[9, 10]. Raymond Davis designed an experiment that used a 380 m 3 tank filled with Perchloroethylene (C_2Cl_4), a dry-cleaning fluid rich in chlorine. Solar neutrinos were expected to change ^{37}Cl to ^{37}Ar via

Table 1: Solar neutrinos from reactions in pp chain (a) and CNO cycle (b).

(a) pp chain		(b) CNO cycle	
solar ν_e	reaction	solar ν_e	reaction
pp	$p + p \rightarrow {}^2\text{H} + e^+ + \nu_e$	CNO	${}^{13}\text{N} \rightarrow {}^{13}\text{C} + e^+ + \nu_e$
pep	$p + e^- + p \rightarrow {}^2\text{H} + \nu_e$		${}^{15}\text{O} \rightarrow {}^{15}\text{N} + e^+ + \nu_e$
hep	${}^3\text{He} + p \rightarrow {}^4\text{He} + e^+ + \nu_e$		${}^{17}\text{F} \rightarrow {}^{17}\text{O} + e^+ + \nu_e$
${}^7\text{Be}$	${}^7\text{Be} + e^- \rightarrow {}^7\text{Li} + \nu_e$		
${}^8\text{B}$	${}^8\text{B} \rightarrow {}^8\text{Be}^* + e^+ + \nu_e$		

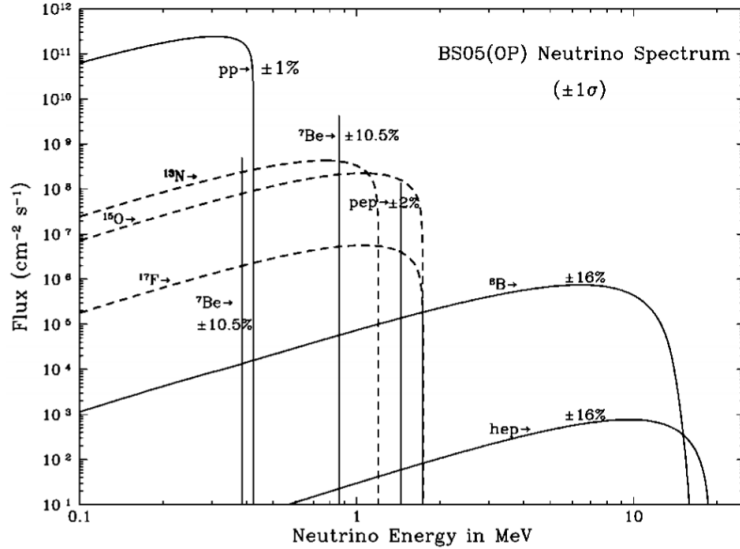


Figure 1: Solar neutrino energy spectrum (E_ν vs. flux) for the solar model BS05(OP)[8].

the endothermic reaction $\nu_e + {}^{37}\text{Cl} \rightarrow {}^{37}\text{Ar} + e^-$ and the produced ${}^{37}\text{Ar}$ were extracted and counted. The neutrino energy threshold (E_{thresh}) of the experiment was 0.814 MeV, which allowed a measurement mostly of the ${}^8\text{B}$ neutrino flux but also including some lower energy neutrinos[10]. Their first results, announced in 1968, showed that only about one-third of the predicted radioactive argon atoms were measured. This raised a problem of missing solar neutrinos.

1.5. Atmospheric Neutrino

Cosmic rays from outer space continuously interact with nuclei in the atmosphere and produce secondary particles. Atmospheric neutrinos come from decay products of the hadrons in the secondaries. The dominant processes of atmospheric ν_e and ν_μ production is $\pi^+ \rightarrow \mu^+ + \nu_\mu$ followed by $\mu^+ \rightarrow e^+ + \bar{\nu}_\mu + \nu_e$. In the 1980s, the Kamiokande experiment in Japan measured atmospheric neutrinos by utilizing a 3-kiloton water-Cherenkov detector. The incoming neutrinos, ν_e (ν_μ) interacted with the water via charged current interactions and electrons (muons) were produced. The electrically charged leptons traversed the water at a speed higher than the speed of light in water and thus emit Cherenkov light, which was recorded by the detector as ring patterns (called Cherenkov rings). The produced electrons caused electro-magnetic showers during their propagation in the water while the produced muons propagated almost in straight lines without producing electro-magnetic showers. Then the ν_μ (the μ -like events) were separated from the ν_e (the e -like events) by the fact that the μ -like events created sharper Cherenkov rings than the e -like events. Kamiokande measured the ratio of fluxes $\Phi(\nu_\mu + \bar{\nu}_\mu)/\Phi(\nu_e + \bar{\nu}_e)$. The fluxes of atmospheric neutrinos are well understood and the ratio ν_μ/ν_e is expected to be ~ 2 at low energies ≤ 1 GeV. In 1988, they found a deficit of measured μ -like events compared to the prediction. This was later confirmed by IMB in 1992[12] and Soudan-2 in 1997[13] and called “atmospheric neutrino anomaly”[14].

2. Neutrino Flavor Mixing and Conversion

2.1. SNO and Super-Kamiokande

The deficit of solar neutrinos and atmospheric neutrinos indicate that a neutrino can change its flavor or oscillate during propagation.

To resolve the solar neutrino problem with a direct approach, Herbert Chen in 1984 proposed an experiment using a large heavy water (D_2O)

Cherenkov detector to distinguish the flavors of solar neutrinos[15]. This proposal lead to the SNO collaboration. The SNO detector was sensitive to the ${}^8\text{B}$ solar neutrinos via three interactions: (1) the charged current (CC): $\nu_e + d \rightarrow e^- + p + p$, (2) the neutral current (NC): $\nu_x + d \rightarrow \nu + p + n$, (3) the elastic scattering (ES): $\nu_x + e^- \rightarrow \nu_x + e^-$. The CC channel was only sensitive to ν_e while the NC channel was independent of the neutrino type, which provided a measurement of the total solar neutrino flux regardless of flavors. The ES channel was also sensitive to all flavors but with reduced sensitivities to ν_μ and ν_τ [16].

In 2002, SNO reported that the measured total ${}^8\text{B}$ solar neutrino flux via the NC channel (Φ_{NC}) was consistent with solar models while the ν_e component of the flux (Φ_e) was about one-third of the total flux[16]. The results reported in 2013 was[17]:

$$P_{SNO} = \frac{\Phi_e}{\Phi_{NC}} = 0.340 \pm 0.023^{+0.029}_{-0.031}$$

The results indicate that about two-thirds of the original solar ν_e have transformed to $\nu_{\mu,\tau}$ when they arrive at earth. This explains the problem of missing solar neutrinos.

In 1996, the Kamiokande experiment was upgraded to a 50-kiloton water Cherenkov detector, Super-Kamiokande (Super-K). In two years, Super-K measured atmospheric neutrinos and announced a striking discovery: the number of high energy muon neutrinos is zenith angle dependent and caused by a deficit of up-going ν_μ [18].

The measured up-going muon neutrinos are mostly created in the atmosphere at the opposite side of the Earth to the Super-K detector and travel about 12800 km while the downward-going muon neutrinos are created in the atmosphere about 15 km above the detector. The measured ν_e in the same scenario do not show such a deficit[18].

Therefore, a natural explanation for the results is that the up-going muon neutrinos have oscillated to ν_τ during their thousands of kilometres travel. The Super-K results are consistent with two-flavor $\nu_\mu \leftrightarrow \nu_\tau$ oscillations[18].

2.2. Flavor Mixing Matrix and Oscillation Probability

Both SNO and Super-K discovered the phenomenon of neutrino flavor conversions directly and were awarded the 2015 Nobel Prize. The phenomenon proves that neutrinos have a small but finite mass, which is not expected in the Standard Model. As early as 1957, Pontecorvo had already

suggested an oscillation of $\nu \leftrightarrow \bar{\nu}$, and later worked out a phenomenological model for $\nu_e \leftrightarrow \nu_\mu$ in theory[19]. In 1962, Ziro Maki, Masami Nakagawa and Shoichi Sakata further introduced a lepton mixing matrix (usually called the PMNS matrix), which is a unitary transformation relating the neutrino flavor and mass eigenstates, as a model for the mixing of different neutrino flavors[6].

The flavor of a neutrino can be taken as a superposition of the mass eigenstates. The two-flavor neutrino mixing model in vacuum is a simplified way to discuss the phenomenon of neutrino flavor conversion.

For a mixing of flavor states ν_e and ν_μ , we have a 2×2 unitary matrix with a mixing angle θ to relate the flavor eigenstates to the mass eigenstates[20]:

$$\begin{bmatrix} \nu_e \\ \nu_\mu \end{bmatrix} = U \begin{bmatrix} \nu_1 \\ \nu_2 \end{bmatrix}, \quad U = \begin{bmatrix} \cos \theta & \sin \theta \\ -\sin \theta & \cos \theta \end{bmatrix}. \quad (2.1)$$

The flavor states evolve in time according to (using natural units, $\hbar = c = 1$):

$$\begin{aligned} |\nu_e(t)\rangle &= \cos \theta e^{-iE_1 t} |\nu_1\rangle + \sin \theta e^{-iE_2 t} |\nu_2\rangle \\ |\nu_\mu(t)\rangle &= -\sin \theta e^{-iE_1 t} |\nu_1\rangle + \cos \theta e^{-iE_2 t} |\nu_2\rangle. \end{aligned} \quad (2.2)$$

Then the probability that a ν_e at time $t_0 = 0$ transforms to a ν_μ at time t is:

$$P_{\nu_e \rightarrow \nu_\mu} = |<\nu_\mu(t)|\nu_e(0)>|^2 = 2 \sin^2 \theta \cos^2 \theta [1 - \cos(E_2 - E_1)t]. \quad (2.3)$$

For ultra-relativistic neutrinos, the momentum magnitude $p \simeq E \gg m$, then $E_1 \simeq p + \frac{m_1^2}{2p}$ and $E_2 \simeq p + \frac{m_2^2}{2p}$, we have $E_2 - E_1 \simeq \frac{m_2^2 - m_1^2}{2p}$, then $P_{\nu_e \rightarrow \nu_\mu}$ can be simplified to be:

$$P_{\nu_e \rightarrow \nu_\mu} = \sin^2(2\theta) \sin^2\left(\frac{m_2^2 - m_1^2}{4E}t\right) = \sin^2(2\theta) \sin^2\left(\frac{\Delta m^2}{4E}L\right), \quad (2.4)$$

where $\Delta m^2 = m_2^2 - m_1^2$. $L = t$ is the distance neutrino travels.

Maximum oscillation occurs at $\frac{\Delta m^2}{4E}L \sim \pi$, which gives an effective length $L^{osc} = 4\pi E / \Delta m^2$.

For a set of units commonly used by experiments, a neutrino with energy E_ν , after flying for a distance of L , has an oscillation probability of:

$$P_{\nu_e \rightarrow \nu_\mu} = \sin^2(2\theta) \sin^2\left(\frac{1.27 \Delta m^2 [eV^2] L [km]}{E_\nu [GeV]}\right). \quad (2.5)$$

The survival probability is defined as:

$$P_{\nu_e \rightarrow \nu_e} = 1 - P_{\nu_e \rightarrow \nu_\mu}. \quad (2.6)$$

2.3. Matter Effects

The matter effect is caused by neutrinos interacting with ambient electrons and nucleons in matter such as the Sun or the Earth. ν_e interacts with electrons via both charged weak current (exchanging W boson) and neutral weak current (Z boson) while ν_μ and ν_τ interact only by the neutral current. The ν_e energy has an addition term, $V_{CC} = \sqrt{2}G_F n_e$, where n_e is the number density of the electrons in matter and G_F is the Fermi coupling constant for the weak interaction. This affects the oscillation probabilities for neutrinos propagating in matter compared to vacuum, which is called the Mikheyev-Smirnov-Wolfenstein (MSW) mechanism[21, 22].

In vacuum two-flavor mixing, the Schrödinger equation can be written (in natural units)[23]:

$$i \frac{d}{dt} \begin{bmatrix} \nu_e \\ \nu_\mu \end{bmatrix} = H_0^f \begin{bmatrix} \nu_e \\ \nu_\mu \end{bmatrix} \quad (2.7)$$

where

$$H_0^f = \begin{bmatrix} -\frac{\Delta m^2}{4E} \cos 2\theta & \frac{\Delta m^2}{4E} \sin 2\theta \\ \frac{\Delta m^2}{4E} \sin 2\theta & \frac{\Delta m^2}{4E} \cos 2\theta \end{bmatrix} + \frac{(m_1^2 + m_2^2)}{2} \begin{bmatrix} 1 & 0 \\ 0 & 1 \end{bmatrix} \quad (2.8)$$

To simplify the calculation, we can drop the second unitary term of H_0^f that is irrelevant to the neutrino flavor conversion. Including the matter effect, we obtain:

$$H_m = \begin{bmatrix} -\frac{\Delta m^2}{4E} \cos 2\theta + \sqrt{2}G_F n_e & \frac{\Delta m^2}{4E} \sin 2\theta \\ \frac{\Delta m^2}{4E} \sin 2\theta & \frac{\Delta m^2}{4E} \cos 2\theta \end{bmatrix} \quad (2.9)$$

We define a mixing angle in matter, θ_m as:

$$\tan 2\theta_m = \frac{\Delta m^2 \sin 2\theta}{\Delta m^2 \cos 2\theta - 2\sqrt{2}EG_F n_e}, \quad (2.10)$$

and define an effective squared-mass difference in matter Δm_m^2 as:

$$\Delta m_m^2 = \sqrt{(\Delta m^2 \cos 2\theta - 2\sqrt{2}EG_F n_e)^2 + (\Delta m^2 \sin 2\theta)^2}. \quad (2.11)$$

In analogy with mixing in vacuum, we can write the mixing equation relating the energy eigenstates in matter (ν_{1m}, ν_{2m}) to the flavor eigenstates with a diagonalized Hamiltonian:

$$\begin{bmatrix} \nu_e \\ \nu_\mu \end{bmatrix} = \begin{bmatrix} \cos \theta_m & \sin \theta_m \\ -\sin \theta_m & \cos \theta_m \end{bmatrix} \begin{bmatrix} \nu_{1m} \\ \nu_{2m} \end{bmatrix}. \quad (2.12)$$

The probability of flavor conversion in matter is:

$$P_{\nu_e \rightarrow \nu_\mu} = \sin^2(2\theta_m) \sin^2 \left(\frac{\Delta m_m^2 L}{4E} \right). \quad (2.13)$$

The denominator in equation (2.10) implies a resonance condition:

$$V(n_e) = \sqrt{2}G_F n_e = \frac{\Delta m^2 \cos 2\theta}{2E}. \quad (2.14)$$

From this condition, for a given E , there is a resonance density n_e^{reson} while for a given n_e , there is a resonance energy E^{reson} . When the resonance condition is satisfied, $\theta_m = \frac{\pi}{4}$ and two flavor neutrinos are maximally mixed, even if the vacuum mixing angle θ is small. This is called matter enhanced neutrino oscillation[21, 24].

2.4. Three-flavor mixing

For three-flavor neutrino mixing, we have[25]:

$$|\nu_f\rangle = \sum_{k=1}^3 U_{fk}^* |\nu_k\rangle, \quad (2.15)$$

where $f = e, \mu, \tau$ and $k = 1, 2, 3$. The unitary PMNS matrix, U_{PMNS} , can be parametrized as: $U_{PMNS} =$

$$\begin{bmatrix} 1 & 0 & 0 \\ 0 & \cos \theta_{23} & \sin \theta_{23} \\ 0 & -\sin \theta_{23} & \cos \theta_{23} \end{bmatrix} \begin{bmatrix} \cos \theta_{13} & 0 & e^{-i\delta_{CP}} \sin \theta_{13} \\ 0 & 1 & 0 \\ e^{-i\delta_{CP}} \sin \theta_{13} & 0 & \cos \theta_{13} \end{bmatrix} \begin{bmatrix} \cos \theta_{12} & \sin \theta_{12} & 0 \\ -\sin \theta_{12} & \cos \theta_{12} & 0 \\ 0 & 0 & 1 \end{bmatrix}. \quad (2.16)$$

In the PMNS matrix, we have four parameters: the three mixing angles θ_{12} , θ_{13} , θ_{23} and the charge-parity (CP) violation parameter of lepton sector, δ_{CP} . The unknown value of δ_{CP} is related to leptogenesis, the hypothetical physical process that produced an asymmetry between leptons and antileptons in the very early universe[26]. In addition, there are two squared-mass differences, $\Delta m_{21}^2 = m_2^2 - m_1^2$ and $\Delta m_{32}^2 = |m_3^2 - m_2^2|$. The sign of Δm_{32}^2 is unknown and it indicates a mass hierarchy problem of whether neutrino mass is normal hierarchy (NH, $m_3 > m_2 > m_1$) or inverted hierarchy (IH, $m_3 < m_1 < m_2$)[25].

Currently, these six parameters have been measured by neutrino oscillation experiments. These experiments can be classified by the neutrino sources

Table 2: Oscillation neutrino experiments.

type	source	E_ν	example
solar	the Sun	MeV scale	SNO
reactor	reactor	MeV scale	DayaBay
atmospheric	cosmic-ray	GeV scale	SuperK
accelerator	ν beam from accelerator	GeV scale	T2K
astronomical	astronomical objects	GeV-EeV scale	IceCube

they use. They are the solar, the reactor, the atmospheric, the accelerator and the astronomical neutrino experiments. Table 2 lists the energy scale of the neutrino source as well as the example experiments.

For the Δm_{21}^2 and θ_{12} , the combined analysis of the measurements from the reactor experiment KamLAND and SNO gave $\Delta m_{21}^2 = 7.59_{-0.21}^{+0.21} \times 10^{-5} eV^2$ and $\tan^2 \theta_{21} = 0.47_{-0.05}^{+0.06}$ [27].

The accelerator neutrino experiments as well as the atmospheric neutrino experiments have measured Δm_{32}^2 and θ_{23} . The most recent results from SuperK show that in NH, $\sin^2 \theta_{23} = 0.588_{-0.064}^{+0.031}$ and $\Delta m_{32}^2 = 2.5_{-0.20}^{+0.13} \times 10^{-3} eV^2$ [28].

In 2012, the reactor neutrino experiment Daya Bay reported the discovery of non-zero θ_{13} with a significance of 5.2σ . In 2016, Daya Bay reported that $\sin^2 2\theta_{13} = 0.0841 \pm 0.0027(stat.) \pm 0.0019(syst.)$. This high-precision result makes $\sin^2 2\theta_{13}$ the best measured mixing angle[29, 30].

δ_{CP} is examined by the experiments which measure the difference between neutrino and antineutrino oscillation probabilities $P(\bar{\nu}_\alpha \rightarrow \bar{\nu}_\beta)$ and $P(\nu_\alpha \rightarrow \nu_\beta)$ [23]. In 2017, the T2K experiment in Japan rejected the hypothesis that neutrinos and antineutrinos oscillate with the same probability at 95% confidence (2σ) level. This indicates a hint of CP symmetry broken by neutrinos[31].

3. Double Beta Decay

For heavy radioactive isotopes with nuclei of even neutron number (N) and even proton number (Z) (called even-even nucleus), beta decay will lead to an odd-odd nucleus which is less stable. For some such isotopes the beta decay is energetically forbidden. In 1935, Maria Goeppert-Mayer pointed

out that they can still decay through a double beta decay process: $(Z, A) \rightarrow (Z+2, A) + 2e^- + 2\nu_e$. This is called ordinary double beta decay or $2\nu\beta\beta$ [32].

In 1937, Ettore Majorana proposed that neutral spin-1/2 particles (fermions) can be their own antiparticles[33]. If neutrinos have this behaviour, the process called neutrinoless double beta decay ($0\nu\beta\beta$) will also be expected. The Feynman diagrams of $2\nu\beta\beta$ and $0\nu\beta\beta$ are illustrated in Figure 2.

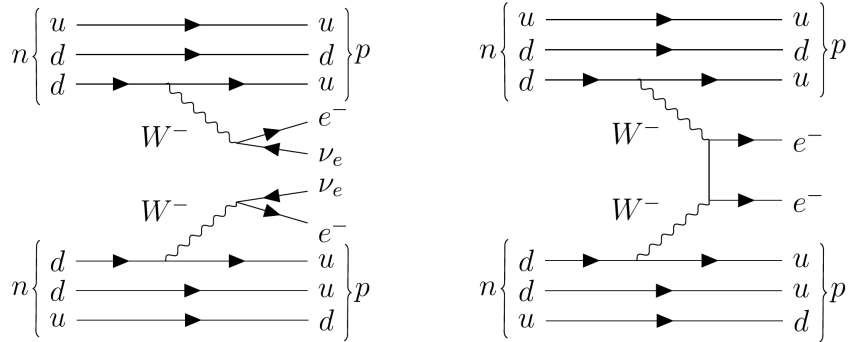


Figure 2: Feynman diagrams for $2\nu\beta\beta$ (left) and $0\nu\beta\beta$ (right).

The interpretation of the $0\nu\beta\beta$ process is considered as exchanging light Majorana neutrinos. In this case the effective Majorana mass $\langle m_{ee} \rangle = \sum_{i=1}^3 |U_{ei}|^2 m_i$ ($i = 1, 2, 3$), U_{ei} are the elements of the neutrino mixing matrix for the flavor state ν_e , and m_i are the mass eigenvalues of the mass eigenstates (from (2.15)). The observable quantity is the half-life:

$$(T_{1/2}^{0\nu\beta\beta})^{-1} = G_{PS} |M_{Nuclear}|^2 \langle m_{ee} \rangle^2,$$

where G_{PS} is the phase space factor and $|M_{Nuclear}|$ is the nuclear matrix element for the physics process describing the $0\nu\beta\beta$ decay process[34].

Similar to beta decay, the $2\nu\beta\beta$ process will cause a continuous spectrum in the detector while the $0\nu\beta\beta$ process only has two electrons in the final state, which sum up to give a distinct energy peak. By measuring this exact energy, a detector with high energy resolution is able to search for the $0\nu\beta\beta$ signal from the $0\nu\beta\beta$ decay radioactive isotopes. Diverse technologies have been developed during the past decades. The following section lists some of the mainstream experiments.

3.1. Status of Double Beta Decay Experiments

The GERmanium Detector Array (GERDA) experiment searches for $0\nu\beta\beta$ of ${}^{76}\text{Ge}$. The experiment uses bare germanium crystals with an enrichment

of up to $\sim 87\%$ ^{76}Ge operated in radiopure cryogenic liquid argon (LAr). In 2017, GERDA reported a 90% confidence level (C.L.) lower limit for the half-life of ^{76}Ge , $T_{1/2}^{0\nu}(^{76}\text{Ge}) > 8.0 \times 10^{25}$ years[35, 36, 37].

The Enriched Xenon Observatory (EXO) experiment uses 200-kg of liquid Xenon (LXe) in a time projection chamber (TPC) to search for $0\nu\beta\beta$ in ^{136}Xe . In 2011 they observed the half life of $2\nu\beta\beta$ of ^{136}Xe to be 2.11×10^{21} years. A limit of $T_{1/2}^{0\nu}(^{136}\text{Xe}) > 1.1 \times 10^{25}$ yr[38] was set in 2014. EXO is now being upgraded to the next 5-ton experiment (nEXO) and is expected to reach an exclusion sensitivity of $T_{1/2}^{0\nu}(^{136}\text{Xe})$ of about 10^{28} years at 90% C.L.[39].

Also using ^{136}Xe , the KamLAND-Zen experiment exploits the existing facilities of KamLAND by setting a 3.08-m-diameter spherical inner balloon filled with 13 tons of Xe-loaded liquid scintillator at the center of the KamLAND detector. Their 2016 results from a $504 \text{ kg}\cdot\text{yr}$ exposure obtained a lower limit for the $0\nu\beta\beta$ decay half-life of $T_{1/2}^{0\nu}(^{136}\text{Xe}) > 1.07 \times 10^{26}$ yr at 90% C.L. and the corresponding upper limits on the effective Majorana neutrino mass are in the range 61-165 meV[40].

The Cryogenic Underground Observatory for Rare Events (CUORE) experiment searches for $0\nu\beta\beta$ in ^{130}Te . CUORE is a tonne-scale cryogenic bolometer array that arranges 988 tellurium dioxide (TeO_2) crystals. CUORE reported first results in 2017 after a total TeO_2 exposure of $86.3 \text{ kg}\cdot\text{yr}$. Combined with their early data, they placed a lower limit of $T_{1/2}^{0\nu}(^{130}\text{Te}) > 1.5 \times 10^{25}$ yr at 90% C.L. and $m_{\beta\beta} < (140 - 400)$ meV[41].

A more recent evaluations of the limits of $T_{1/2}^{0\nu}$ and $m_{\beta\beta}$ from the above mentioned experiments are summarized in Table 3[37].

Table 3: The limits of $T_{1/2}^{0\nu}$ and $m_{\beta\beta}$ at 90% C.L.

Experiment	Isotope	Limit of $T_{1/2}^{0\nu}$ (10^{25} year)	Limit of $m_{\beta\beta}$ (eV)
GERDA	^{76}Ge	>8.0	$<0.12\text{-}0.26$
KamLAND-Zen	^{136}Xe	>10.7	$<0.05\text{-}0.16$
EXO	^{136}Xe	>1.1	$<0.17\text{-}0.49$
CUORE	^{130}Te	>1.5	$<0.11\text{-}0.50$

4. SNO+ Experiment

The SNO+ experiment is the successor of the SNO experiment, which makes use of the SNO detector structure. Located in SNOLAB at a depth of 2 km from the surface, the rock overburden is about 6000 meter water equivalent (m.w.e), which greatly reduces the cosmic muon backgrounds. The detector consists of an acrylic vessel (AV) sphere of 12 m in diameter and 5.5 cm in thickness. The AV sphere is concentric within a 17.8 m diameter stainless steel sphere, which holds 9438 photomultipliers (PMT). These two structures are housed in a rock cavity filled with 7000 tonnes of ultra-pure water (UPW) to provide both buoyancy for the vessel and radiation shielding[42, 43].

The SNO+ detector is designed for multi-purpose measurements of neutrino physics. The experiment will go through three phases[42]:

1. Water phase

The AV was filled with about 900 tonnes of ultra-pure water. The detector has been collecting physics data since May 2017.

The main physics goal in this phase is to search for the invisible nucleon decay, which violates baryon number and is a prediction of Grand Unified Theory (GUT). In this decay mode, ^{16}O decays into $^{15}\text{O}^*$ or $^{15}\text{O}^*$, which de-excites and produces a γ ray of about 6 MeV.

During the water phase, different types of calibration runs have been taken. The detector responses, systematics and backgrounds are studied. Multiple physics analyses of solar neutrinos, reactor antineutrinos and nucleon decay are going on. The external backgrounds are also measured, which will be the same as the following two phases.

2. Scintillator phase

The AV will be filled with 780 tonnes of liquid scintillator, which is a mixture of linear alkylbenzene (LAB) as a solvent and 2 g/L of 2,5-diphenyloxazole (PPO) as a fluor.

In this phase, the main physics goal is to measure low energy solar neutrinos: the CNO, pep and low energy ^8B neutrinos. The pep neutrinos are mono-energetic, with $E_\nu=1.442$ MeV and their flux is well predicted by the Standard Solar Model. A measurement of the pep neutrinos will give more information of the matter effects in neutrino oscillations[44].

The solar metallicity is the abundance of elements heavier than ^4He (called “metal” elements in the context of astronomy). It is poorly constrained and the predictions from different solar models disagree with each

other. A measurement of the CNO neutrinos can give the abundance of ^{12}C , ^{13}N and ^{15}O and can thus resolve the metallicity problem[45].

Geoneutrino, reactor antineutrino and supernova neutrino detections are additional goals.

A six-month period of scintillator filling and six to twelve months of data-taking are expected for this phase. During the filling, it is planned to operate the partially filled detector at a water level about 4.4 m for about two weeks. This partial filled transition phase is mainly aimed to understand the in-situ backgrounds of scintillator.

3. Tellurium loading phase

In this final phase, natural Tellurium will be loaded into the scintillator, in which ^{130}Te is a double beta decay isotope. The main purpose in this phase is searching for $0\nu\beta\beta$ in ^{130}Te .

5. My Work on SNO+

5.1. Reconstruction for SNO+ Water Phase

To study the physics events in the SNO+ detector, a reconstruction algorithm (fitter) is needed to obtain the position, direction and time of an event. A Multi-path Fitter (MPF) framework was developed by the Alberta group as an alternative fitter to the SNO+ official fitter. In this framework, fitters for SNO+ water phase (MP Water Fitter), wavelength shifter (MP WLS Fitter) and partial-fill phase (MP Partial Fitter) were developed. In SNO+ water phase, the cavity and the AV are both filled with pure water. This is a relatively simple geometry. Therefore, we start with the MP Water Fitter to explain the reconstruction concepts.

The MP Water Fitter uses prompt light and assumes that photons propagate in straight lines (straight light paths) for likelihood calculations. Detailed situations, such as the reflection and lensing effects from different detector components are neglected. Figure 3 shows the reconstruction concepts for position and direction.

In the left panel of Figure 3, when an event happens at a position of \vec{X}_0 , photons are emitted and propagate to PMTs. The triggered PMTs at known positions \vec{X}_{PMT} record the time when they are fired (t_{PMT}). The time residual is defined by:

$$t_{\text{res}} = t_{\text{PMT}} - \frac{|\vec{X}_0 - \vec{X}_{\text{PMT}}|}{v_{gr}} - t_0, \quad (5.1)$$

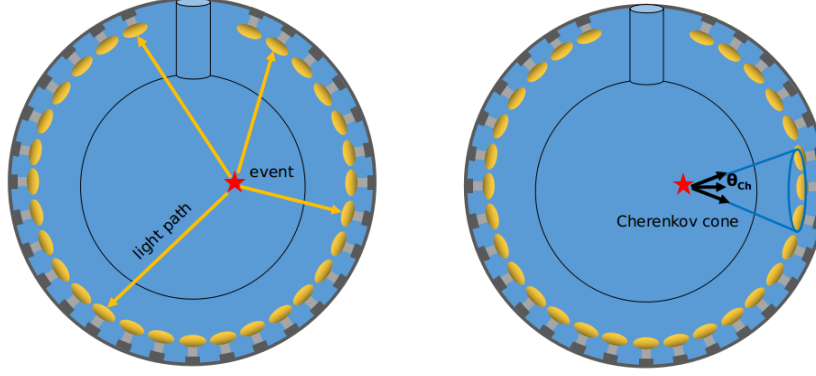


Figure 3: Diagrams of position reconstruction (left) and direction (right).

where t_0 is the event time and v_{gr} is an averaged group velocity of light.

For all the triggered PMTs, the likelihood is built by $L = \prod_{i=0}^{NHit} P_i(t_{res})$, where $NHit$ is the number of triggered PMTs and P_i is the calculated probability for the i -th triggered PMT based on t_{res} . The PMT response time of a certain event in a certain detector medium, which is based on measurements and simulations, is used as a probability density function (pdf). The fitter varies the trial vertex of event position \vec{X}_0 and event time t_0 , (\vec{X}_0, t_0) to calculate the likelihood function. By maximizing the likelihood, the best-fit vertex is found.

For the MP Water Fitter, the pdf is the measured PMT response time modified by the photon propagation time in the water, as shown in the left panel of Figure 4.

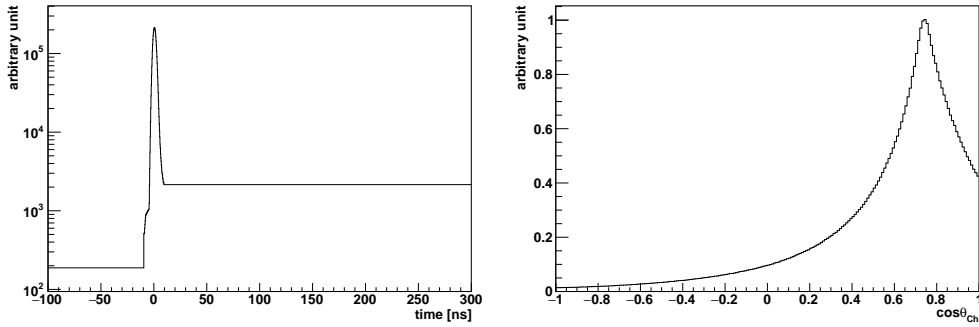


Figure 4: The pdfs for the MP Water Fitter. Left: timing pdf. Right: angular distribution pdf.

A cone of Cherenkov photons is created along the charged particle momentum \vec{p} , or the direction of the particle, $\hat{n} = \vec{p}/|\vec{p}|$. The light cone is detected on the PMT sphere, forming a Cherenkov ring. For a known (or best-fit) \vec{X}_0 and triggered PMT position \vec{X}_{PMT} , the angle θ_{cone} between $(\vec{X}_{\text{PMT}} - \vec{X}_0)$ and \hat{n} is calculated by:

$$\cos \theta_{\text{cone}} = \frac{(\vec{X}_{\text{PMT}} - \vec{X}_0) \cdot \hat{n}}{|\vec{X}_{\text{PMT}} - \vec{X}_0|}.$$

The θ_{cone} should be close to the Cherenkov angle θ_{Ch} . This is illustrated in the right panel of Figure 3. From Monte Carlo (MC) simulations of electrons travelling along the same direction (positive x axis, $+x$) in the pure water, we extract a distribution of $\cos \theta_{Ch}$ (angular distribution), as shown in the right panel of Figure 4. It is peaked at $\cos \theta_{Ch} \approx 0.75$ ($\theta_{Ch} \approx 41.4^\circ$), which is the same as the water Cherenkov angle $\cos \theta_{Ch} = 1/1.33$.

5.2. Reconstruction for Water-based Wavelength Shifter

There was a proposal of adding wavelength shifter (WLS) into the SNO+ detector during the water phase. The specific wavelength shifter we considered is PPO, which will be used in the SNO+ scintillator phase and Te-loaded phase. Although the proposal will not happen for SNO+ due to the experiment schedule, it is still worthwhile for a conceptual study of a SNO+-like detector that uses water-based wavelength shifter (wbWLS) as medium. The advantage of a wbWLS detector is to increase the light yield while still keeping the directionality. This technology is being studied by some future solar neutrino experiments, such as the Advanced Scintillation Detector Concept (ASDC)[46, 47].

Figure 5 shows the position distributions of triggered PMTs for MC simulated 5 MeV electrons travelling along $+x$ direction in the AV. The left panel shows the case when the detector is filled with pure water while the right panel is for water plus 0.1 ppm PPO. For the same electrons, the number of triggered PMTs (N_{Hit}) in wbWLS is about 2.4 times greater than the pure water one. Although there is extra isotropic light emitted, the Cherenkov ring can still be seen clearly, allowing reconstruction of the directionality.

Figure 6 shows the energies of simulated electrons as a function of the mean value of the N_{Hit} distribution (mean nhits). In pure water, a 1 MeV electron simulation does not trigger any PMTs while in wbWLS case we have a mean nhits of 20.

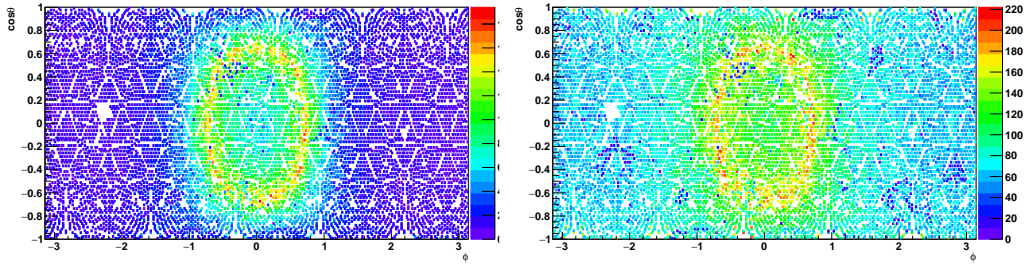


Figure 5: Position distributions of triggered PMTs (in zenith and azimuth angles) for 5 MeV electrons travelling along $+x$ direction in the pure water (left) and the water plus 0.1 ppm PPO (right).

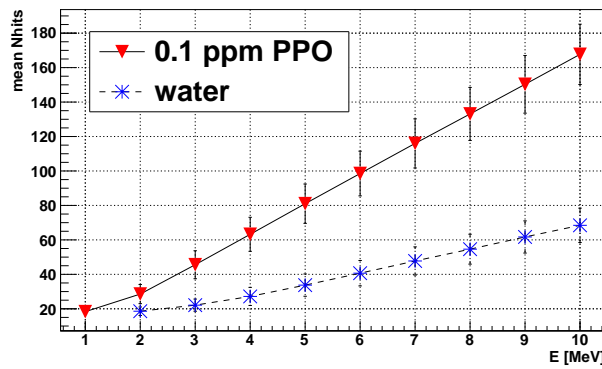


Figure 6: The energies of simulated electrons as a function of mean nhits. The values in the 0.1 ppm PPO (solid line with inverted triangle) are compared with the water (dashed line with star).

In the wbWLS case, since WLS absorbs and re-emits photons, the reconstruction mentioned in section 5.1 is slightly modified to build the MP WLS Fitter. According to the optical property of PPO, the prompt light emitted from an event has a probability of ~ 0.6 to be absorbed by the WLS and then re-emitted at a shifted vertex along the particle direction \hat{n} . Then the fitter returns a shifted vertex, $\vec{X}_{0,\text{shifted}} = \vec{X}_0 + \text{offset} \cdot \hat{n}$. The offset we set in the fitter is 100 mm obtained from simulations. Figure 7 shows the timing pdf for the wbWLS, which is the PMT response time modified to photon propagation time in the wbWLS.

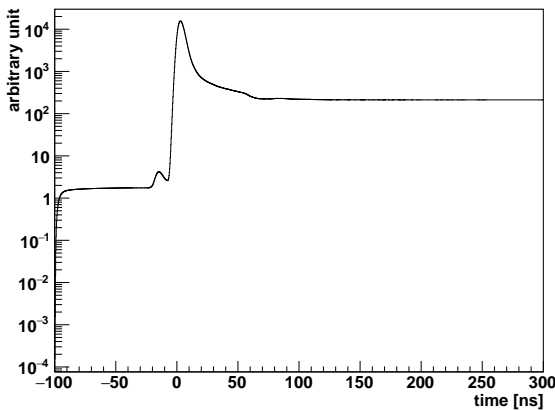


Figure 7: The timing pdf for the wbWLS.

To reconstruct the direction, besides the angular distribution of Cherenkov photons, $\cos \theta_{Ch}$, we also consider the fraction of the re-emitted and wavelength shifted photons that cause a flat angular distribution.

To test the performance of the MP WLS Fitter, 5 MeV electrons were simulated at the center of the AV filled with wbWLS and travelling along $+x$ direction. As a comparison, the same simulation was done for the AV filled with pure water and the simulated events were reconstructed by the water fitter.

Figure 8 shows the performance of the WLS fitter reconstructed positions of the MC simulations compared to the pure water case. For the fit position distribution of 5 MeV electrons in the wbWLS, we get a root mean square (RMS) of 201 mm and a bias to the center (the mean of histogram) of 29 mm. Compared to the pure water case, the fit bias is about 19 mm better and the RMS is 188 mm better.

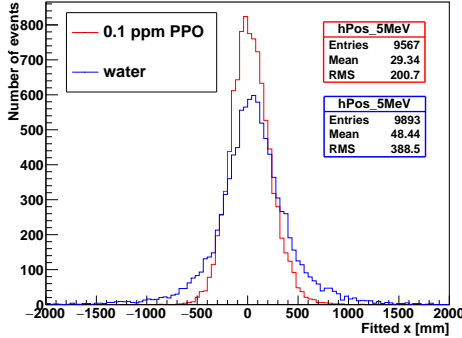


Figure 8: Fit position projected on x axis. The WLS fitter reconstructed x positions of the 5 MeV electron events in the wbWLS (red) are compared to the ones in the water (blue).

For a given Cherenkov event, the error in the reconstructed event direction is defined as[48]: $\cos(\theta_e) = \vec{u}_{fit} \cdot \vec{u}_e$, where \vec{u}_e is the simulated electron direction and \vec{u}_{fit} is the reconstructed direction. To quantify this error, we define a $\cos \theta_a$ so that:

$$\frac{\int_{\cos \theta_a}^1 P(\cos \theta_e) d \cos \theta_e}{\int_0^1 P(\cos \theta_e) d \cos \theta_e} = a.$$

where $P(\cos \theta_e)$ is the distribution of $\cos \theta_e$ from MC data. The value of $\cos \theta_a$ is found numerically to let $\cos \theta_e$ contain $a \cdot 100\%$ of the reconstructed data. A larger $\cos \theta_a$ means better direction reconstruction.

Table 4 shows the results of $\cos \theta_a$ for SNO heavy water data[48] and simulations for SNO+ pure water and wbWLS.

Table 4: A comparison of quantitative estimates for the angular resolution between the SNO heavy water, SNO+ wbWLS and the SNO+ pure water cases.

medium	$\cos \theta_{0.9}$	$\cos \theta_{0.8}$	$\cos \theta_{0.5}$
SNO heavy water	0.50	0.71	0.92
SNO+ water	0.53	0.76	0.93
wbWLS	0.37	0.63	0.90

Comparing a pure water SNO+ detector and the wbWLS one, using the MP WLS Fitter for physics events gives a better position resolution without

a significant loss in the performance of the direction reconstruction.

5.3. Testing the Fitter with SNO+ ^{16}N Calibration

During the water phase, a Nitrogen-16 (^{16}N) calibration source was deployed for calibration scans in June and November, 2017 and March, 2018.

The ^{16}N calibration runs provide an ideal test of fitter performance. From a comparison of reconstructions for data and MC, we can also extract the resolution and bias of the fitter.

The γ rays emitted from the ^{16}N source interact with the water in the detector mainly via Compton scattering. Figure 9 shows the spatial distributions of the first γ -ray interaction positions projected on the x axis (called spatial distribution $S(x)$) obtained from MC simulation. The ^{16}N source is considered as an electron source with a known spatial distribution[48]. For simplicity, in the following we always discuss the x component of the position vector \vec{X} .

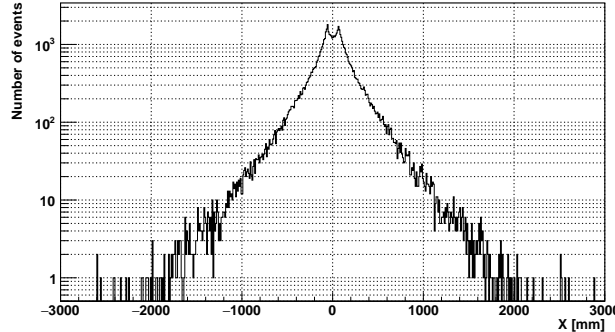


Figure 9: Spatial distributions of ^{16}N first γ -rays interaction position projected on x axis, obtained from simulations.

A position resolution function is defined for the reconstructed electron position distribution[48]:

$$R(x) = \frac{1 - \alpha_e}{\sqrt{2\pi}\sigma_p} \exp\left[-\frac{1}{2}\left(\frac{x - \mu_p}{\sigma_p}\right)^2\right] + \frac{\alpha_e}{2\tau_p} \exp\left[\frac{-|x - \mu_p|}{\tau_p}\right],$$

where α_e is the fractional exponential component, σ_p is the Gaussian width (corresponding to the position resolution), μ_p is the Gaussian shift (corresponding to the position bias) and τ_p is the exponential slope (corresponding to the position distributions in tails).

For electrons from the ^{16}N calibration source, their spatial distribution function $N_R(x)$ can be described by the position resolution function smeared by the convolution of $S(x)$ as[48]:

$$N_R(x) = \int_{-\infty}^{+\infty} S(x) R(x_{fit} - x) dx.$$

Since the $S(x)$ and $N_R(x)$ are histograms obtained from the data and MC, we calculate by the bin value x_i :

$$N_R(x_i) = \sum_{x_i=-\infty}^{+\infty} S(x_i) R(x_{fit}^i - x_i).$$

The χ^2 is calculated by:

$$\chi^2 = \sum_{i=0}^{N_{bins}} \left[\frac{N_R(x_{fit}^i) - N_R^{fit}(x_{fit}^i)}{\sigma_i} \right]^2,$$

where N_R^{fit} is a trial fit to the N_R by tuning the $\{\alpha_e, \mu_p, \sigma_p, \tau_p\}$ and σ_i is taken as the bin width of the histograms.

By minimizing the χ^2 , the parameters of the resolution function, $\{\alpha_e, \mu_p, \sigma_p, \tau_p\}$ and a best N_R^{fit} are obtained.

Figure 10 shows a comparison of the reconstructed x position of ^{16}N events between data and MC. The reconstructed position distributions are fitted with N_R^{fit} .

Table 5 summarizes the values of position resolution parameters obtained from data and MC of ^{16}N calibration runs at the detector center.

Table 5: Position resolution parameters for the MP Water Fitter.

MPW fitter	α_e	σ_P (mm)	τ_P (mm)	μ_P (mm)
data	0.58 ± 0.04	175.8 ± 3.8	288.0 ± 5.7	-28.8 ± 1.0
MC	0.51 ± 0.05	195.2 ± 3.3	298.4 ± 6.1	-10.9 ± 1.0

5.4. Reconstruction for SNO+ Partial-fill Phase

The MP Partial Fitter was developed for the partial-fill phase to reconstruct the event position and time.

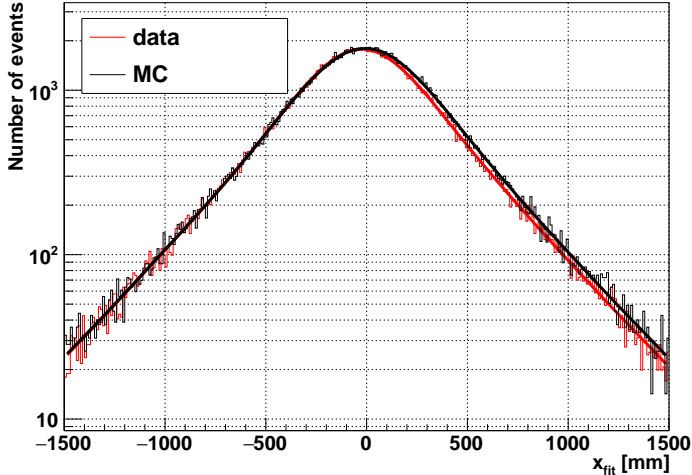


Figure 10: Distributions of the reconstructed position projected on x axis, obtained from SNO+ ^{16}N central run data (red) and MC (black). The distributions are fitted with N_R^{fit} (red and black lines).

In the partial fill geometry, photons will travel with different speeds as they pass through two different mediums, water and scintillator. Assuming a straight light path, the MP Partial Fitter mainly calculates the total length of the light path ($|\vec{l}_p| = |\vec{X}_{\text{PMT}} - \vec{X}_0|$) and separates it into the lengths in scintillator (d_{sp}) and in water ($|\vec{l}_p| - d_{sp}$).

As illustrated in Figure 11, a detailed calculation of d_{sp} includes evaluations of (1) light path and neck (line-cylinder) intersection; (2) light path and AV sphere (line-sphere) intersection and (3) light path and water-scintillator interface (line-plane) intersection. d_{sp} is further separated into the path length in neck ($d_{sp,neck}$) and in AV ($d_{sp,AV}$).

Then the time of flight is obtained by:

$$tof = \frac{|\vec{l}_p| - d_{sp}}{v_{gr,water}} + \frac{d_{sp}}{v_{gr,scint}}, \quad (5.2)$$

The time residual is $t_{res} = t_{\text{PMT}} - tof - t_0$.

If $d_{sp} = 0$, the light path is always in the water. In this case, the fitter is the same as the MP Water Fitter. The fitter fits with the MP Water Fitter pdf. Once the light path passes through the scintillator region, the fitter fits with a scintillator timing pdf, the PMT time response modified to photon

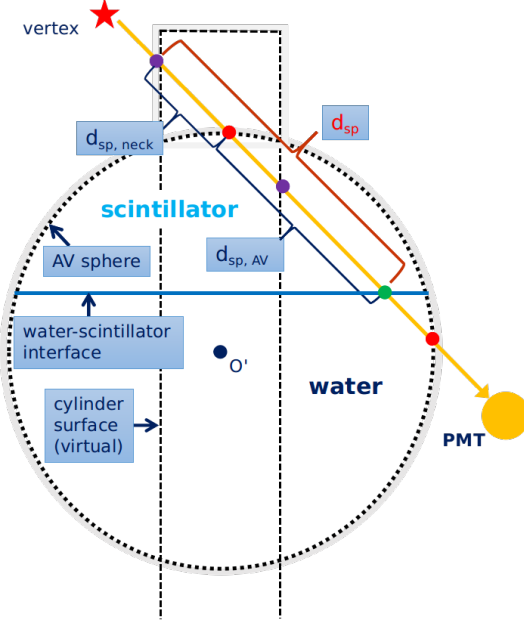


Figure 11: Light path calculation for the MP Partial Fitter.

propagation time in scintillator, as shown in Figure 12.

The performance of the fitter was studied with MC simulations. In a partial fill geometry with water level at 4.4 m, 2.5 MeV electrons are simulated inside the AV in the scintillator region only, the water region only and the whole AV region.

Figure 13 and Figure 14 show the MP Partial Fitter reconstructed results for these simulations. Figure 13 shows the biases between the fit positions and MC positions, projected on the x axis. The distributions of position biases are fit with Gaussian functions. The values of Gaussian mean and sigma quantify the fit biases and resolutions. Table 6 lists these values.

Table 6: Reconstructed position biases and resolutions for simulated events in partial fill.

regions of simulated events	bias (mm)	resolution (mm)
scintillator region	-1.0	73.9
water region	-10.7	385.1
full region	6.9	331.72

For the events in water, the fit bias and resolution is comparable to the

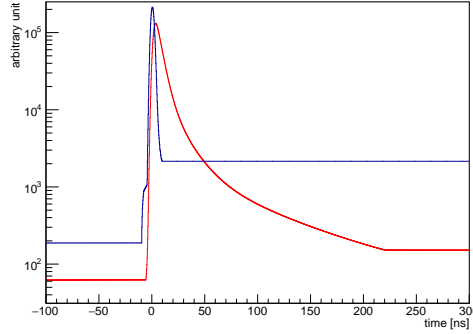


Figure 12: The timing pdfs used by the MP Partial Fitter. Blue: the timing pdf used by the MP Water Fitter; Red: the scintillator timing pdf.

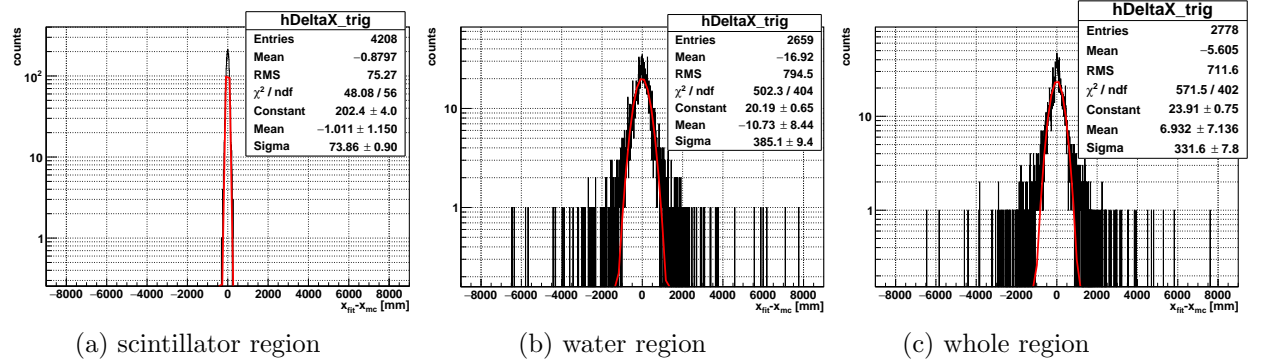


Figure 13: Distributions of fit position bias projected on x axis ($x_{fit} - x_{MC}$).

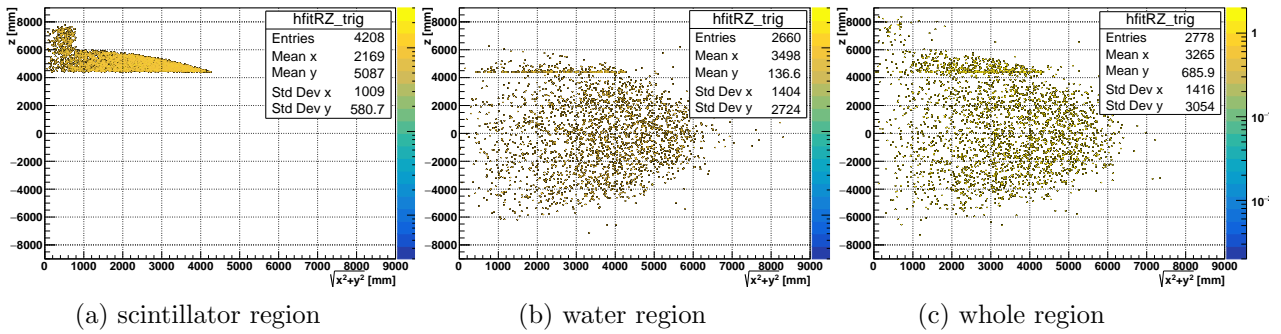


Figure 14: Fit results: $\rho_{fit} = \sqrt{x_{fit}^2 + y_{fit}^2}$ vs. z_{fit} .

water phase results in Table 5. The events in the scintillator region have smaller fit bias and better resolution due to more triggered PMTs in the reconstruction.

Figure 14 shows the fit $\sqrt{x^2 + y^2}$ vs. fit z positions. It shows that the fitter can distinguish different events in the water or scintillator region. The fitter gives reasonable results of the three different MC simulations.

6. Thesis Research Plan

October to November, 2018: My work is focusing on the further development of the reconstruction algorithm related to the partial fill and scintillator phases. The accuracy and speed of the MP Partial Fitter are being improved. The fitter will be tested on MC simulations of backgrounds. Based on the reconstructed results of the simulations, the methods of event classification as well as the cuts for distinguishing signals from backgrounds will be developed.

November, 2018 to Spring, 2019: In this period, I will analyze the partial fill data and the scintillator phase data with the reconstruction algorithms I am developing. The analyses will focus on an understanding of the backgrounds and searching for solar neutrino signals. ^{238}U is one of the natural radioisotopes found in the scintillator[49]. It goes through a series of radioactive decays, called decay chain, which produces different radioisotopes. These radioisotopes may mimic the solar neutrino signals. One focus of the background analysis is to determine the level of ^{238}U in the scintillator. The solar neutrino analysis will focus on the methods of signal extraction and the evaluations of solar neutrino events.

I will start writing my thesis in summer, 2019.

References

- [1] <https://en.wikipedia.org/wiki/Neutrino>

- [2] Anderson, E.C. The Reines-Cowan Experiments.
<http://permalink.lanl.gov/object/tr?what=info:lanl-repo/lareport/LA-UR-97-2534-02>
- [3] H. Bethe and R. Peierls. The ‘neutrino’. *Nature*, 133:5321934.
- [4] <http://hyperphysics.phy-astr.gsu.edu/hbase/Particles/cowan.html>
- [5] Bethe, Hans Albrecht. “Energy production in stars.” *Physical Review* 55.5 (1939): 434.
- [6] Giunti, Carlo, and Chung W. Kim. *Fundamentals of neutrino physics and astrophysics*. Oxford university press, 2007.
- [7] W. C. Haxton et al. “Solar neutrinos: status and prospects.” *Ann. Rev. Astron. Astrophys.*, 51:21, 2013
- [8] Bahcall, John N., Aldo M. Serenelli, and Sarbani Basu. “New solar opacities, abundances, helioseismology, and neutrino fluxes.” *The Astrophysical Journal Letters* 621.1 (2005): L85.
- [9] Bahcall, John N. “Solar neutrinos. i. theoretical.” *Physical Review Letters* 12.11 (1964): 300.
- [10] Davis Jr, Raymond. “Solar neutrinos. ii. experimental.” *Physical Review Letters* 12.11 (1964): 303.
- [11] Bahcall, John N. “Gallium solar neutrino experiments: Absorption cross sections, neutrino spectra, and predicted event rates.” *Physical Review C* 56.6 (1997): 3391.
- [12] Becker-Szendy, R., Bratton, C.B., Casper, D., Dye, S.T., Gajewski, W., Goldhaber, M. et al. (1992) Electron- and muon-neutrino content of the atmospheric flux. *Phys. Rev. D* 46, 3720-3724.
- [13] Allison, W.W.M., Alner, G.J., Ayres, D.S., Barrett, W.L., Bode, C., Border, P.M. et al. (Soudan-2 collaboration) (1997) Measurement of the atmospheric neutrino flavour composition in Soudan 2. *Phys. Lett. B* 391, 491-500.

- [14] Takaaki Kajita, “Atmospheric Neutrinos,” Advances in High Energy Physics, vol. 2012, Article ID 504715, 24 pages, 2012. doi:10.1155/2012/504715
- [15] Chen, Herbert H. “Direct approach to resolve the solar-neutrino problem.” Physical Review Letters 55.14 (1985): 1534.
- [16] Ahmad, Q. Retal, et al. “Direct evidence for neutrino flavor transformation from neutral-current interactions in the Sudbury Neutrino Observatory.” Physical review letters 89.1 (2002): 011301.
- [17] Aharmim, B., et al. “Combined analysis of all three phases of solar neutrino data from the Sudbury Neutrino Observatory.” Physical Review C 88.2 (2013): 025501.
- [18] Fukuda, Y., et al. “Evidence for oscillation of atmospheric neutrinos.” Physical Review Letters 81.8 (1998): 1562.
- [19] “The Nobel Prize in Physics 2015”. Nobelprize.org. Nobel Media AB 2014. Web. 1 Oct 2017. http://www.nobelprize.org/nobel_prizes/physics/laureates/2015/
- [20] Cahn, Robert N., and Gerson Goldhaber. The experimental foundations of particle physics. Cambridge University Press, 2009.
- [21] Smirnov, A. Yu. “Solar neutrinos: Oscillations or No-oscillations?” arXiv preprint arXiv:1609.02386 (2016).
- [22] Smirnov, A. Yu. “The MSW effect and matter effects in neutrino oscillations.” Physica Scripta 2005.T121 (2005): 57.
- [23] Xing, Zhizhong, and Shun Zhou. Neutrinos in particle physics, astronomy and cosmology. Springer Science & Business Media, 2011.
- [24] Fukugita, Masataka, and Tsutomu Yanagida. Physics of Neutrinos: and Application to Astrophysics. Springer Science & Business Media, 2013.
- [25] M. Tanabashi et al. (Particle Data Group), Phys. Rev. D 98, 030001 (2018).
- [26] [https://en.wikipedia.org/wiki/Leptogenesis_\(physics\)](https://en.wikipedia.org/wiki/Leptogenesis_(physics))

- [27] Abe, S., et al. “Precision measurement of neutrino oscillation parameters with KamLAND.” Physical Review Letters 100.22 (2008): 221803.
- [28] Abe, Kazutaka, et al. “Atmospheric neutrino oscillation analysis with external constraints in Super-Kamiokande I-IV.” Physical Review D 97.7 (2018): 072001.
- [29] An, Feng Peng, et al. “Measurement of electron antineutrino oscillation based on 1230 days of operation of the Daya Bay experiment.” Physical Review D 95.7 (2017): 072006.
- [30] Qian, Xin, and Jen-Chieh Peng. “Physics with Reactor Neutrinos.” arXiv preprint arXiv:1801.05386 (2018).
- [31] Abe, K., et al. “Measurement of neutrino and antineutrino oscillations by the T2K experiment including a new additional sample of ν_e interactions at the far detector.” Physical Review D 96.9 (2017): 092006.
- [32] Martin, Brian R. Nuclear and particle physics: an introduction. John Wiley & Sons, 2006.
- [33] Majorana, Ettore, and Luciano Maiani. “A symmetric theory of electrons and positrons.” Ettore Majorana Scientific Papers. Springer, Berlin, Heidelberg, 2006. 201-233.
- [34] Zuber, Kai. “Neutrinoless double beta decay.” arXiv preprint nucl-ex/1201.4665v1 (2012).
- [35] Agostini, M., et al. “Search of Neutrinoless Double Beta Decay with the GERDA Experiment.” Nuclear and Particle Physics Proceedings 273 (2016): 1876-1882.
- [36] Agostini, M., et al. “Background-free search for neutrinoless double- β decay of 76 Ge with GERDA.” Nature 544.7648 (2017): 47.
- [37] Agostini, M., et al. “Improved Limit on Neutrinoless Double- β Decay of Ge 76 from GERDA Phase II.” Physical review letters 120.13 (2018): 132503.
- [38] Albert, J. B., et al. “Search for Majorana neutrinos with the first two years of EXO-200 data.” Nature 510.7504 (2014): 229.

- [39] Albert, J. B., et al. “Sensitivity and Discovery Potential of nEXO to Neutrinoless Double Beta Decay.” arXiv preprint arXiv:1710.05075 (2017).
- [40] Gando, A., et al. “Search for Majorana neutrinos near the inverted mass hierarchy region with KamLAND-Zen.” Physical review letters 117.8 (2016): 082503.
- [41] Alduino, C., et al. “First Results from CUORE: A Search for Lepton Number Violation via $0\nu\beta\beta$ Decay of ^{130}Te .” arXiv preprint arXiv:1710.07988 (2017).
- [42] Andringa, S., et al. “Current Status and Future Prospects of the SNO+.” Advances in High Energy Physics 2016 (2016).
- [43] Erica Caden for the SNO+ Collaboration. “Status of the SNO+ Experiment.” arXiv preprint arXiv:1711.11094 (2017).
- [44] Davini, S., et al. “CNO and pep solar neutrino measurements and perspectives in Borexino.” Journal of Physics: Conference Series. Vol. 675. No. 1. IOP Publishing, 2016.
- [45] Cerdeno, David G., et al. “CNO neutrino Grand Prix: the race to solve the solar metallicity problem.” Journal of Cosmology and Astroparticle Physics 2018.04 (2018): 037.
- [46] Dai, Xiongxin, et al. “Wavelength shifters for water Cherenkov detectors.” Nuclear Instruments and Methods in Physics Research Section A: Accelerators, Spectrometers, Detectors and Associated Equipment 589.2 (2008): 290-295.
- [47] Alonso, J. R., et al. “Advanced scintillator detector concept (ASDC): a concept paper on the physics potential of water-based liquid scintillator.” arXiv preprint arXiv:1409.5864 (2014).
- [48] Boulay, Mark Guy. Direct evidence for weak flavour mixing with the Sudbury Neutrino Observatory. 2001.
- [49] Langrock, Stefanie. Measurement of the Rayleigh Scattering Length and Background contributions during early data taking phases at SNO+. Diss. Queen Mary University of London, 2017.